J. Fluid Mech. (1975), *vol.* 71, *part* 4, *pp.* 675–687
Printed in Great Britain

Secondary convection in a Hele Shaw cell

By LLOYD L. GREEN AND THEODORE D. FOSTER
Scripps Institution of Oceanography, La Jolla, California 92093

(Received 23 January 1975)

A convective instability is produced by salt water diffusing onto the surface of a fresh-water layer in a Hele Shaw cell. Although the horizontal wavelength of the initial instability is small, an increase in the horizontal wavelength of the convective flow with time and depth is observed as the resulting two-dimensional convection develops. The phenomenon of wavelength variation is confirmed numerically, but quantitative observational and theoretical comparison is limited to small Rayleigh numbers. It is shown that perturbations in the density field cause horizontal pressure gradients, which in turn cause convective elements to combine.

1. Introduction

Free vertical convection occurs when a thermal or salinity boundary layer becomes statically unstable. The fluid motion resulting from the instability is a vastly more effective transport mechanism than molecular diffusion alone. Convective elements separated by tens or hundreds of metres are commonly observed in the atmosphere as thermals and cumulus clouds. Large convective features have also been documented in the ocean from current-meter records (Medoc Group 1970) and from infrared photos of the sea surface (McAlister & McLeish 1965).

In the laboratory, streamers formed at the onset of convection in layers deep compared with the diffusive boundary layer have a horizontal spacing of the order of millimetres for salt (Foster 1969*a*) and centimetres for heat (Foster 1965*a*). Foster (1965*b*) has shown that if the fluid is sufficiently deep (i.e. at a sufficiently high Rayleigh number) the thickness of the diffusive boundary layer, rather than the total depth of the fluid layer, determines the initial horizontal wavelength. The boundary-layer thickness is determined by fluid properties which are the same in laboratory experiments as in nature. Thus the results of laboratory experiments in such 'deep' layers should be applicable to geophysical phenomena at high Rayleigh number, and the natural onset of convection should also occur on a millimetre or centimetre scale. There must therefore be mechanisms for the growth from these millimetre or centimetre scales to the wavelengths of tens or hundreds of metres found in nature. In this paper we shall discuss one mechanism for the combination of convective streamers into elements of larger wavelength.

In order to examine a simple convective system that could be investigated both in the laboratory and numerically, we chose the convection of salt in a

Hele Shaw cell. This system has several advantages. First, the Hele Shaw cell is a tank such that one dimension is so small compared with the others that the flow is essentially two-dimensional. This presents an obvious advantage for numerical computations. It also allows the experiments to be easily observed using a shadowgraph for flow visualization, and results in photographs of the flow pattern which are much less ambiguous than those taken using normal tanks. Second, salt was chosen to drive the convection instead of heat because in a Hele Shaw cell the ratio of the exposed surface to the fluid volume is very great, and therefore heat losses through the cell surfaces would be difficult to take into account. Third, the effective viscosity of the fluid in a Hele Shaw cell depends upon the gap width, and this gives an easily controlled parameter through which the system may be examined.

2. Mathematical theory

For a Hele Shaw cell the Navier–Stokes equation becomes (Lamb 1932, p. 582)

$$\rho\left(\frac{\partial \mathbf{v}}{\partial t}+\mathbf{v}.\nabla\mathbf{v}\right)=-\nabla p+\rho g\hat{\mathbf{z}}-\frac{12\mu}{l^2}\mathbf{v}, \tag{1}$$

where $\hat{\mathbf{z}}$ is in the direction of gravity, μ is the viscosity of the fluid and l is the separation of the cell walls. We consider only the case of a vertical Hele Shaw cell with two-dimensional flow in the x, z plane. The conservation of salt is given by

$$\partial S/\partial t+\mathbf{v}.\nabla S=D\nabla^2 S, \tag{2}$$

where S is the salinity and D the diffusivity.

We assume an incompressible fluid,

$$\nabla.\mathbf{v}=0, \tag{3}$$

and a linear equation of state of the form

$$\rho=\rho_0(1+\gamma S). \tag{4}$$

ρ_0 is the density at zero salinity and γ the coefficient of haline contraction.

The equations are made non-dimensional using as length, velocity, time and salinity scales h, D/h, h^2/D and ΔS respectively, where h is the depth of the fluid layer and ΔS the initial salinity difference across the top of the layer. Substituting the equation of state into (1) and taking the curl to eliminate the pressure gradient, we obtain

$$\frac{\delta^2}{\tilde{\sigma}}\nabla\times\left[(1+\gamma S\Delta S)\left(\frac{\partial \mathbf{v}}{\partial t}+\mathbf{v}.\nabla\mathbf{v}\right)\right]=-\tilde{R}\frac{\partial S}{\partial x}\hat{\mathbf{y}}-\nabla\times\mathbf{v}, \tag{5}$$

where we have defined the modified kinematic viscosity as $\tilde{\nu}=12\mu/\rho_0$, the modified Schmidt number as $\tilde{\sigma}=\tilde{\nu}/D$, the ratio of the plate separation to the layer depth as $\delta=l/h$ and the modified Rayleigh number as $\tilde{R}=\gamma g\Delta S l^2 h/\tilde{\nu}D$. (For a constant salt difference the Rayleigh number is proportional to the depth of the fluid layer.) Since the modified Schmidt number is very large and δ very small, the inertial terms are small compared with both the viscous and the buoyancy

terms and can be neglected. Thus the system is nonlinear owing only to the advection of salt, and vorticity is created by local salinity gradients. Equation (5) then becomes

$$-\left(\frac{\partial u}{\partial z}-\frac{\partial w}{\partial x}\right)=\tilde{R}\frac{\partial S}{\partial x}, \tag{6}$$

where u and w are the x and z velocities. If we define the stream function ψ such that $u=-\partial\psi/\partial z$ and $w=\partial\psi/\partial x$ satisfy the continuity equation, (6) becomes

$$\nabla^2\psi=\tilde{R}\,\partial S/\partial x. \tag{7}$$

This equation was solved simultaneously with the salt equation

$$\frac{\partial S}{\partial t}-\frac{\partial\psi}{\partial z}\frac{\partial S}{\partial x}+\frac{\partial\psi}{\partial x}\frac{\partial S}{\partial z}=\nabla^2 S. \tag{8}$$

The boundary conditions are chosen such that the velocities normal to the boundaries are zero; thus $\psi=0$ at $z=0,1$, $x=0,m$, where m is the non-dimensional width of the tank. We assume constant salinity at the top, zero salinity at the bottom, and no flux of salt through the sides; thus $S=1$ at $z=0$, $S=0$ at $z=1$ and $\partial S/\partial x=0$ at $x=0,m$. The surface condition is reasonable because of the large size of the salt-water reservoir. The bottom boundary condition should actually be a no-flux requirement, but because the numerical model was not run long enough for streamers to impinge on the bottom, no appreciable error results.

3. Numerical model

There are several features of our physical system that pose problems in numerical simulation. First, advection and diffusion of salt are physically important, so that any time-stepping scheme must be stable with both terms present. Second, there can be difficulty in spatially resolving the surface boundary layer, which can be as small as 10^{-3} cm thick. Third, the initial millimetre-scale streamers must be resolved, and numerically this problem is intimately related to the initial perturbation of the flow.

The salinity equation was time stepped with a predictor–corrector second-order scheme (Hamming 1962, chap. 14) which is stable to both advection and diffusion. First, the predictor uses a centred time step to estimate the salinity field at an advanced time. Then this estimate is corrected by a modified forward time step employing the average of the time derivatives of S at the present and advanced time. (Computation of the advanced derivative requires solving the vorticity equation for an estimate of ψ at the future time.) The difference between the predicted and corrected values gives an approximation to the error in the salinity field. The error estimate is first used to 'mop up' or modify the corrector value, and then, if the error exceeds 5 % of the surface salinity, to decrease the time step. The vorticity equation is then resolved and the process is repeated with a new predictor time step. Note that the vorticity equation must be solved twice for each step but that increased stability is achieved. During the time stepping the Jacobian is computed by the Arakawa (1966) second-order nine-point

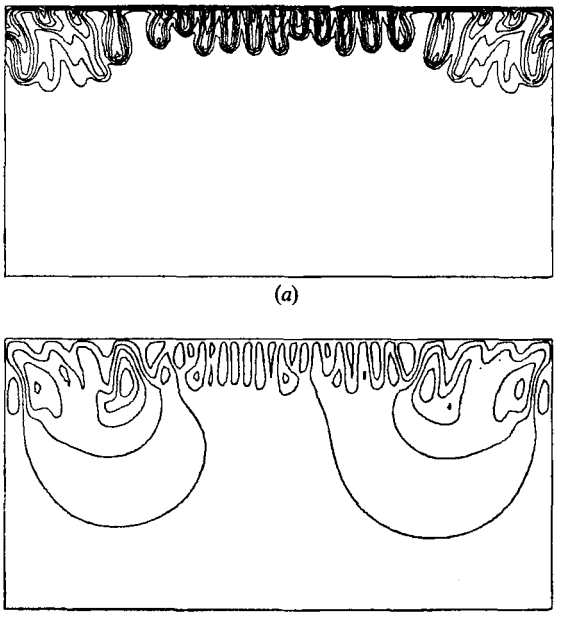

FIGURE 1. (*a*) Isohalines and (*b*) streamlines at a non-dimensional time $1{\cdot}77 \times 10^{-3}$.

method and the Laplacian by the standard five-point finite-difference representation (Gerald 1970, p. 193). The Jacobian conserves mean-square vorticity and total energy from grid point to grid point, but cannot eliminate the aliasing error (i.e. the inability to resolve features smaller than the grid spacing).

A direct approach was used for solution of Poisson's equation for the vorticity. Again, the centred and five-point difference representations were used, resulting in a sparse matrix for the equation. One can then use the truncated Buneman algorithm to reduce the number of equations and to solve them directly (Buzbee, Golub & Nielson 1970). This algorithm was found to save a substantial amount of computer time compared with the successive over-relaxation method.

The boundary layer was resolved by taking a sufficient number of vertical points to eliminate non-physical effects such as negative salinity values or streamers that were flattened on the bottom. A useful criterion was to make the uniform grid small enough for the salinity at the first grid point below the surface to be about 0·8 of the surface salinity at the onset of convection.

The system was perturbed by giving random values to the top row of the stream-function field. The values were uniformly distributed between $\pm 10^{-3}$, being four orders of magnitude less than those in fully developed flow. The highest frequency that can be introduced and resolved is determined by the number of horizontal points. The number of points was increased until the number of streamers no longer changed. Resolution required 5–6 points per roll or 10–12 points per streamer. The initial wavelength is not unique, because of the 'lock in' effect described by Foster (1969*b*), in that the initial number of streamers is dependent on the initial perturbation. This effect was evident for large initial perturbations,

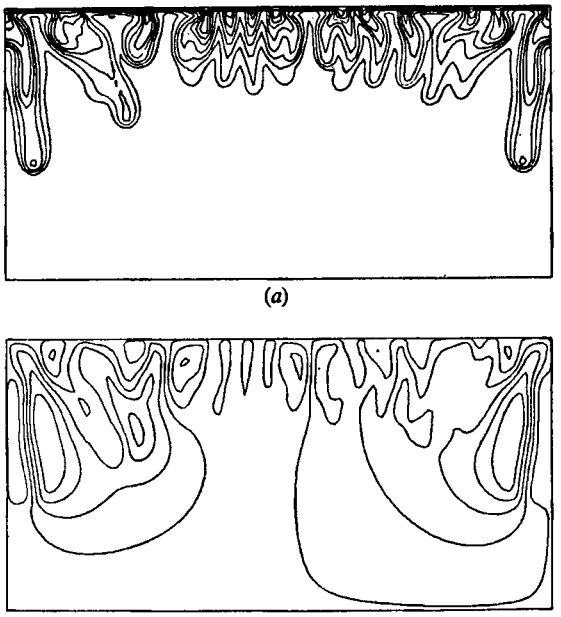

(*a*)

(*b*)

FIGURE 2. (*a*) Isohalines and (*b*) streamlines at a non-dimensional time $2{\cdot}41 \times 10^{-3}$.

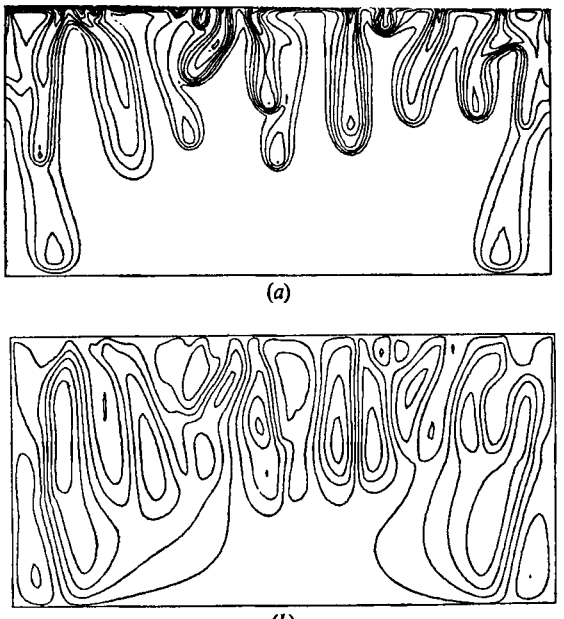

(*a*)

(*b*)

FIGURE 3. (*a*) Isohalines and (*b*) streamlines at a non-dimensional time $3{\cdot}49 \times 10^{-3}$.

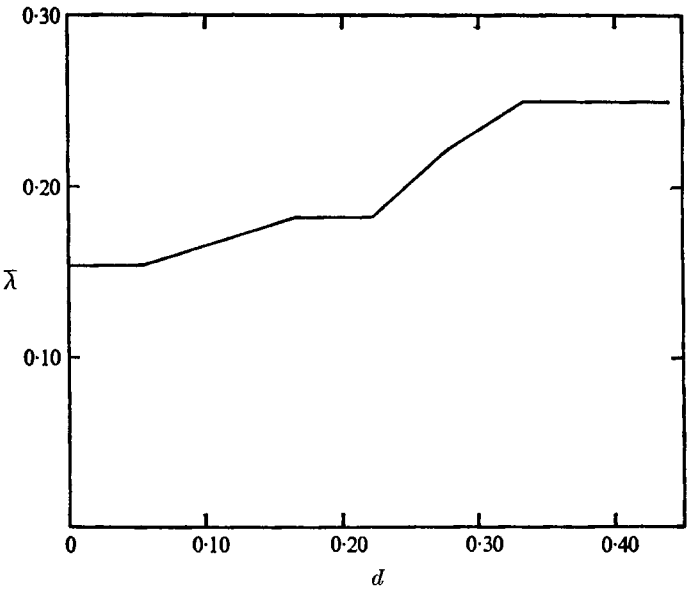

FIGURE 4. Non-dimensional calculated values of the average horizontal wavelength *vs* depth at a non-dimensional time $3{\cdot}49 \times 10^{-3}$.

but using a small random initial disturbance, it was found to give an uncertainty of only plus or minus a single streamer or approximately 5 % in the average initial wavelength.

4. Numerical results

The salinity and stream-function fields have been calculated for $\tilde{R} = 2{\cdot}63 \times 10^3$. Isohalines and streamlines are shown in figures 1, 2 and 3 for a layer 1 non-dimensional unit deep by 2 wide at times of $1{\cdot}77 \times 10^{-3}$, $2{\cdot}41 \times 10^{-3}$ and $3{\cdot}49 \times 10^{-3}$. For a tank spacing of 0·013 cm and a surface salinity of 25‰ the layer would be 1·4 cm deep by 2·8 cm wide and the convection simulated at 239, 325 and 471 s.

The full onset of convection is observed at a time $1{\cdot}77 \times 10^{-3}$ after the system is perturbed (figure 1). The first instability occurs adjacent to the lateral boundaries and the figure shows that several initial convective elements have begun to combine to form large boundary streamers. Boundary effects ultimately perturb about half of the flow. The onset of convection at the centre is slightly non-uniform owing to the randomness of the initial perturbation. The stream function shows that the longest streamers have begun to curve under shorter adjacent elements. At a time $2{\cdot}41 \times 10^{-3}$ after the perturbation, pairs of streamers shown in figure 2 have begun to combine by drifting laterally and diffusing together. The process is accentuated by the tendency of streamers to flow under each other. Lateral drift can be seen by comparing the positions of the streamers at times of $1{\cdot}77 \times 10^{-3}$ and $2{\cdot}41 \times 10^{-3}$. A comparison of the stream functions at these times shows that the mean horizontal wavelength has increased with time and that several cells have strengthened. The mechanism of wavelength growth can

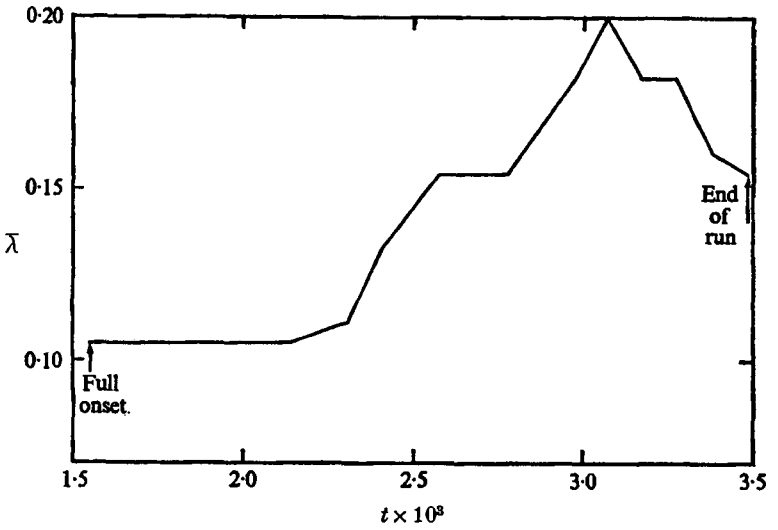

FIGURE 5. Non-dimensional calculated values of the average horizontal wavelength at the surface *vs.* non-dimensional time.

be seen clearly from the salinity isolines at a time of $3{\cdot}49 \times 10^{-3}$. Extended streamers flow around, and thus combine with, adjacent shorter streamers as observed in the initial stages of the convection. The process ultimately relies on lateral diffusion for the combination of convective elements. The onset of convection at the surface is limited by updrafts or return circulation between the large streamers, so that the horizontal wavelength at the surface increases with time. However, new streamers continue to form except in areas of the boundary layers where there are very strong updrafts.

The increase in the average horizontal wavelength with depth is quantified by dividing the horizontal distance by the number of streamers at several depths. Streamers are considered to have joined when they flow together, but fine-structure may still be distinguishable in the larger elements. The variation in wavelength with depth is shown in figure 4 for a time of $3{\cdot}49 \times 10^{-3}$. The simulation represents about a 0·2 cm wavelength change in the top 0·8 cm of the tank for a plate separation of the Hele Shaw cell of 0·01 cm.

Figure 5 shows that there is an increase in the average horizontal wavelength at the surface with time up to a time of about $3{\cdot}0 \times 10^{-3}$ owing to the updrafts advecting away the boundary layer. Then the horizontal wavelength starts to decrease as streamers reform in areas where the updrafts have weakened and the boundary layer thickened. The wavelength probably would reach, or oscillate about, a quasi-steady value if the run were continued indefinitely.

5. Experimental apparatus and measurement techniques

The experimental apparatus is shown in figure 6. The Hele Shaw cell was constructed of two vertical 1·9 cm thick pieces of plate glass separated by greased seals at the edges and bottom. The dimensions were approximately 57·2 cm high

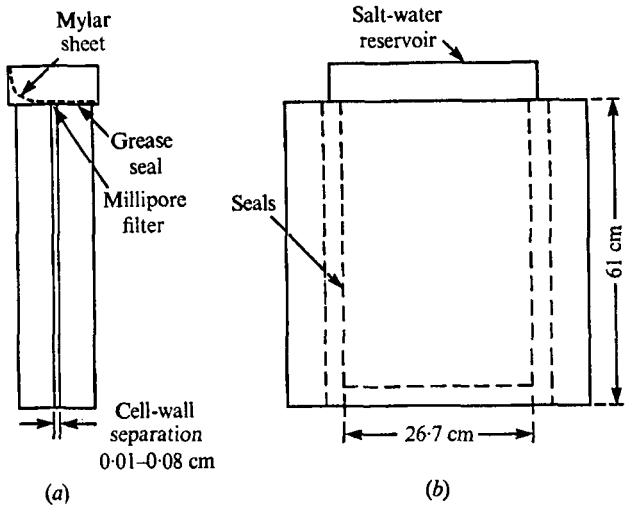

FIGURE 6. Schematic diagram of the Hele Shaw cell. (a) End view. (b) Front view.

by 26·7 cm wide. Experiments using wall separations from 0·01 to 0·08 cm were performed. A tank of about 700 ml capacity was sealed to the top of the cell to provide a reservoir for the salt solution. The salt water was constrained to diffuse through a strip of Millipore filter at the bottom of the upper tank. (The uniform 5 μm matrix of the Millipore was found to yield a very uniform source of salt water at the top of the cell.) Experiments were initiated by removing a Mylar sheet separating the salt-water reservoir and the cell below. Experiments were performed using sodium chloride solutions with concentrations from 6 to 200‰.

The convection was observed using a parallel-beam shadowgraph optical system (Beams 1954). The light source was a 100 W mercury arc lamp focused on a slit placed at the focal length of the first mirror so that a parallel beam passed through the tank. The mirrors were parabolic astronomical mirrors of diameter 32 cm and focal length 254 cm ground to $\frac{1}{4}$ wavelength accuracy and placed about 630 cm apart. The deflexion of the parallel beam was proportional to the second derivative of the index of refraction as it passed through the tank, resulting in dark and light areas at the camera. Either a 35 mm reflex still camera or 16 mm motion picture camera was used to photograph the development of the convection (the latter at 1 frame/s). Frames were enlarged for measurement of the wavelength of the convective streamers. Some error was introduced into the observations since the system must be operated slightly out of focus. Also, the mirror size in our parallel-beam configuration limits the field of view to about the upper 20 cm of the tank.

6. Experimental results

The experimental photographs have much the same appearance as the calculated salinity profiles discussed earlier, but comparison of the two is limited. Computer storage limits the numerical model to a maximum modified Rayleigh

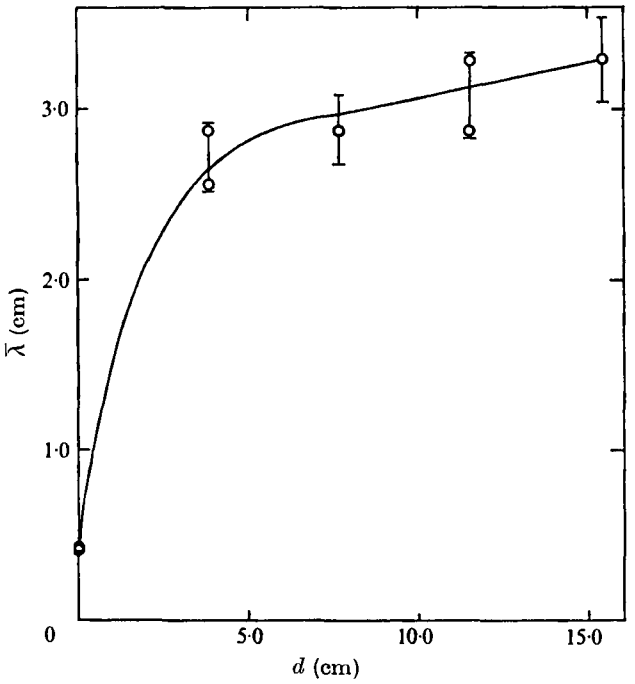

FIGURE 9. The average wavelength *vs.* depth for a cell-wall separation of 0·076 cm and salinity of 25‰ 429 s after the onset of convection.

number $\tilde{R} = 2{\cdot}63 \times 10^3$. This corresponds to a layer 1·4 cm deep by 2·8 cm wide for the minimum experimental salinity and tank gap. (The minimum usable salinity (25‰) is limited by the sensitivity and resolution of the shadowgraph, while the minimum tank thickness (0·01 cm) is constrained by large uncertainties in measurement of the gap and imperfections in the glass.) Somewhat larger values of l and ΔS make the initial unstable boundary layers too small to be experimentally observable. Thus the numerical and experimental results can be compared only for the limiting case, but larger Rayleigh numbers can be considered experimentally.

Figure 7 (plate 1) shows the onset of convection for the limiting case of a gap width $l = 0{\cdot}013$ cm at a salinity $\Delta S = 25$‰. The average wavelength at the surface is $0{\cdot}18 \pm 0{\cdot}03$ cm but this may be an overestimate owing to combination of streamers. Numerical predictions give 0·15 cm for this case, which, considering the errors in both the numerical and experimental work, seems to be in good agreement.

Figures 8(*a*)–(*e*) (plates 1–3) show the mechanism of wavelength growth for $l = 0{\cdot}076$ cm and $\Delta S = 25$‰ at 45 s intervals after the start of the run. The flow is initiated as small streamers, but these begin to drift horizontally and diffuse together. Small elements are elongated and therefore forced to diffuse more rapidly as they become fine-structure within larger sinking streamers. The longer streamers curve under and combine with shorter elements in a fashion similar to the numerical results. The combination can be seen most clearly in figures 8(*c*),

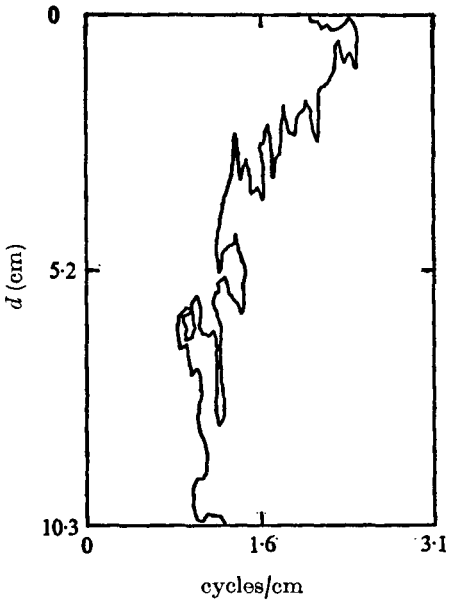

FIGURE 10. A level of constant energy on a plot of depth *vs.* cycles/cm in real tank dimensions for a cell-wall separation of 0·076 cm and salinity of 25‰ 120 s after onset.

(*d*) and (*e*) at 135, 180 and 225 s, respectively. Note that streamers will also occasionally split after several have combined (figure 8*e*). This may be due to asymmetry in the buoyancy after combination. However, the new streamers were observed later to recombine with adjacent elements, so that the overall result was an increase in wavelength with depth. This process was observed in the numerical simulation for the cells adjacent to the boundary streamers. These elements bifurcated and then half of them joined the boundary flow.

The average wavelength was computed by counting the number of streamers within a centred horizontal segment about 24 cm long and dividing by this distance (the entire width of the tank was not used in computing $\bar{\lambda}$ in order to limit edge effects). Figure 9 shows the increase in wavelength with depth for $l = 0{\cdot}076$ cm and $\Delta S = 25‰$ 429 s after onset. A change from 0·43 to 3·2 cm is observed in the upper 15 cm of the tank, but the greatest change occurs in the upper 4 cm. Part of the rapid change near the surface is due to the fact that the fine-structure within a streamer is ignored when computing $\bar{\lambda}$.

An increase in wavelength with depth is also found by spectral analysis performed for $l = 0{\cdot}076$ cm and $\Delta S = 25‰$ 120 s after the onset of convection. The film was scanned with a digitizing microdensitometer connected to an on-line computer. The scanner window was set to resolve density variations within less than 1 mm in real tank dimensions. When corrected for the film response, this procedure yielded a 256×256 grid of 8 bit intensity values for the film, which were automatically converted into 256 horizontal spectra. Since the shadowgraph responds as the second derivative of the index of refraction, these spectra were divided by the square of the frequency to give index-of-refraction spectra. The final spectra were then vertically averaged 10 rows at a time. Figure 10

shows a level of constant energy on a plot of depth *vs.* cycles/cm in real tank dimensions. In this case the cells extend about 6 cm down the tank and in this region the wavenumber decreases. The apparent increase in wavenumber near the surface is a result of the convolution used for vertical averaging of spectra and does not appear to be real.

The numerical results are not applicable to the onset of convection in this case because the predicted wavelength of the streamers is less than the thickness of the tank, and Hele Shaw theory does not apply. However, after the streamers have grown larger than the tank gap the theory is applicable, and the qualitative behaviour is similar to the numerical results.

The experimental as well as the numerical results show an effect of the general circulation on the onset of convection at the surface. The small change in the surface value of $\bar{\lambda}$ with time shown by the numerical results is difficult to detect within experimental uncertainty. However, figure 8 shows that large separations occur at points of upward return flow between large streamers. It was observed that, if a new streamer forms at a point of upward flow, it is often swept laterally to combine with a larger element.

7. Conclusion

The onset of vertical convection at high Rayleigh numbers occurs at wavelengths related to the boundary-layer thickness, but experimental and numerical results have shown that the initial convective streamers can combine to form larger convective elements. Combination occurs when streamers drift horizontally and diffuse together. Adjacent streamers can also flow together at their ends, cutting off the upward flow between them and allowing the elements to combine along their entire length. Quantitative comparison of the experimental and theoretical wavelengths could only be achieved for relatively small Rayleigh numbers, and agreement was found in this case. Somewhat larger boundary streamers were observed at the ends of the Hele Shaw cell in the numerical results as well as in the experiments. However, in the numerical work, unlike the experiments, they dominated the small region that could be simulated. The salt cannot diffuse across the ends of the Hele Shaw cell, which may increase the buoyancy of the boundary streamers in relation to other streamers. The influence of the lateral boundaries on the interior flow would probably be small for the large number of streamers that occurred at the onset of convection in our experiments.

The combination of convective streamers can be investigated from an overall energy viewpoint and from the mechanics of streamer interaction. Convective systems tend to maximize heat (or salt) transfer for high Rayleigh numbers, where the system approaches turbulent conditions and loses the influence of its past history (Malkus 1954). In our system the larger streamers are more efficient in transferring salt and thus according to this principle should be favoured. This can be seen heuristically in that the diffusion of salt is proportional to the circumference of the projected area of a streamer, and hence smaller streamers lose salt (and thus buoyancy) faster relative to their volume than larger streamers. Thus

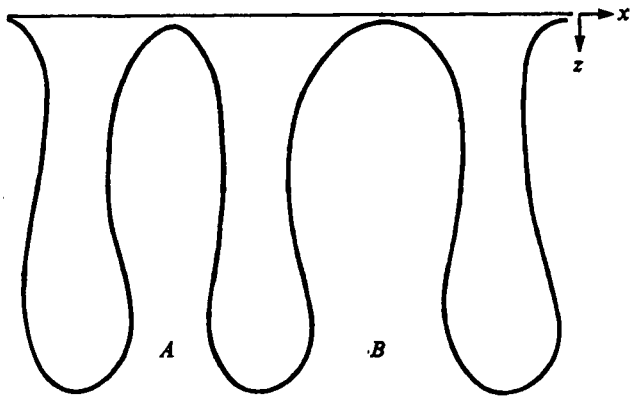

FIGURE 11. Schematic diagram of three convective streamers of slightly uneven horizontal separation.

larger streamers fall faster and transfer salt more rapidly by convection than smaller streamers.

The mechanics of streamer combination involve horizontal pressure gradients developed by differences in the upward flow, thus making the system unstable to perturbations in the horizontal wavelength. This can be seen by examining the equations of motion. The time-dependent and inertial terms were found to be small in our earlier analysis, so that (1) can be written in component form as

$$\frac{\partial p}{\partial x} = -\frac{12\mu}{l^2}u, \quad \frac{\partial p}{\partial z} = \rho g - \frac{12\mu}{l^2}w. \tag{9), (10}$$

Consider a system that has been perturbed in wavelength as shown in figure 11. Little is known about the density within a streamer so we apply (10) to points A and B between convective elements. Integrating (10), we obtain

$$p(z) = \rho_0 gz - \frac{12\mu}{l^2}\int_0^z w(z)\,dz, \tag{11}$$

where the first term on the right is the same at A and B. As we saw above, larger streamers have higher speeds than smaller streamers. The same should be true for the rising fresh-water elements. Thus the upward speeds in region B should be larger than those in region A. The larger fresh-water elements *were* observed to rise faster both in the laboratory and in the numerical experiments. The compression of streamlines in the centre of figure 2(*b*) shows that the higher upward speeds occur where the separation of streamers is the greatest. Since the velocity is lower at B than at A (i.e. more negative), (11) shows that the pressure at B must be higher. The horizontal pressure gradient will move the central streamer in figure 11 left, towards its neighbour, at a rate given by (9). Therefore there is an instability mechanism for producing larger elements by the combination of smaller elements which seems to be in accord with both our laboratory and numerical experiments.

We should like to thank M. C. Hendershott for his advice on numerical modelling, F. H. Busse and C. W. Van Atta for their criticism of an earlier version of this paper, and J. L. Harris for his assistance in obtaining spectral data. We are indebted to the Office of Naval Research for financial support.

REFERENCES

ARAKAWA, A. 1966 Computational design for long-term numerical integration of the equations of fluid motion: two-dimensional incompressible flow. *J. Comp. Phys.* **1**, 119.

BEAMS, J. W. 1954 Shadow and schlieren methods. In *Physical Measurements in Gas Dynamics and Combustion*, p. 26. Princeton University Press.

BUZBEE, B. L., GOLUB, G. H. & NIELSEN, C. W. 1970 On direct methods for solving Poisson's equations. *SIAM J. Numer. Anal.* **7**, 627.

FOSTER, T. D. 1965*a* Onset of convection in a layer of fluid cooled from above. *Phys. Fluids*, **8**, 1770.

FOSTER, T. D. 1965*b* Stability of a homogeneous fluid cooled uniformly from above. *Phys. Fluids*, **8**, 1249.

FOSTER, T. D. 1969*a* Experiments on haline convection induced by the freezing of sea water. *J. Geophys. Res.* **74**, 6967.

FOSTER, T. D. 1969*b* The effect of initial conditions and lateral boundaries on convection. *J. Fluid Mech.* **37**, 81.

GERALD, C. F. 1970 *Applied Numerical Analysis.* Addison–Wesley.

HAMMING, R. W. 1962 *Numerical Methods for Scientists and Engineers.* McGraw-Hill.

LAMB, H. 1932 *Hydrodynamics*, 6th edn. Cambridge University Press.

MCALISTER, E. D. & MCLEISH, W. L. 1965 Oceanic measurements with airborne infrared equipment and their limitations. In *Oceanography from Space* (ed. G. C. Ewing), p. 189. Woods Hole Oceanographic Institution, Ref. 65–10.

MALKUS, W. V. R. 1954 The heat transport and spectrum of thermal turbulence. *Proc. Roy. Soc.* A **225**, 196.

MEDOC GROUP 1970 Observations of the formation of deep water in the Mediterranean Sea. *Nature*, **227**, 1037.

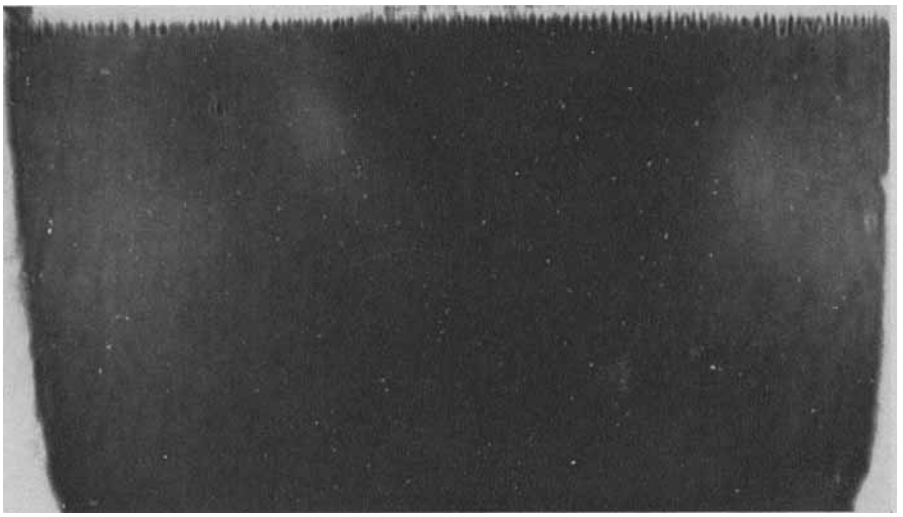

FIGURE 7. Onset of convection for a cell-wall separation of 0·013 cm at a salinity of 25‰. The horizontal field of view is 26·7 cm.

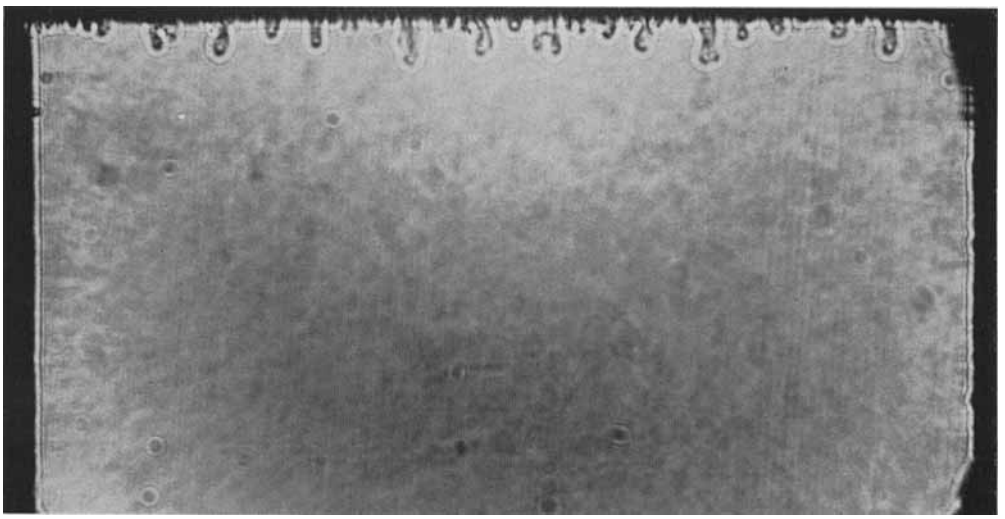

FIGURE 8 (*a*). For caption see plate 3.

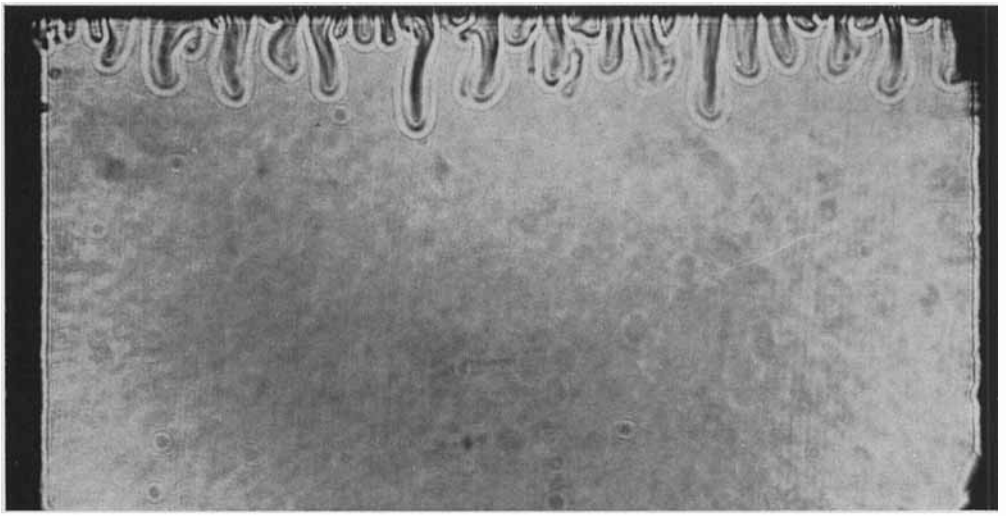

(*b*)

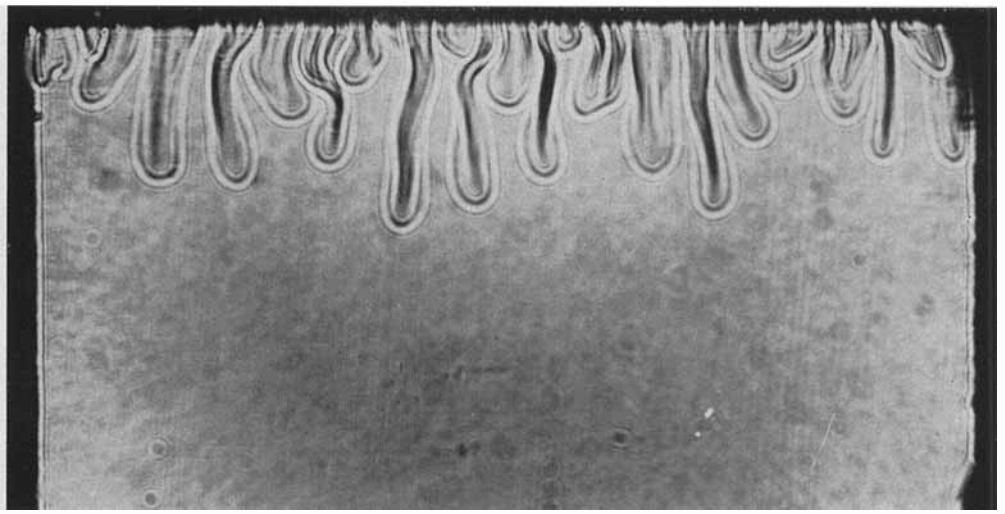

(*c*)

FIGURES 8 (*b*, *c*). For caption see plate 3.

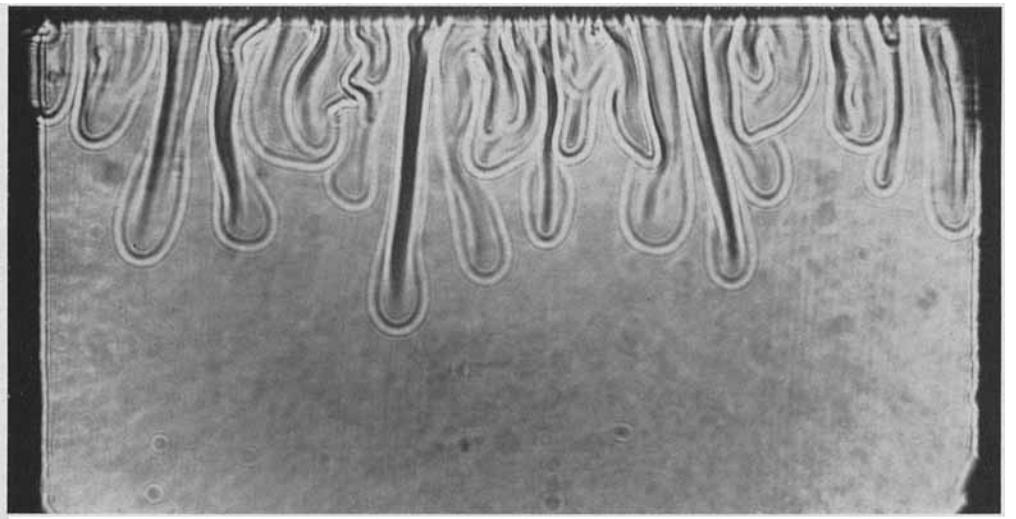

(*d*)

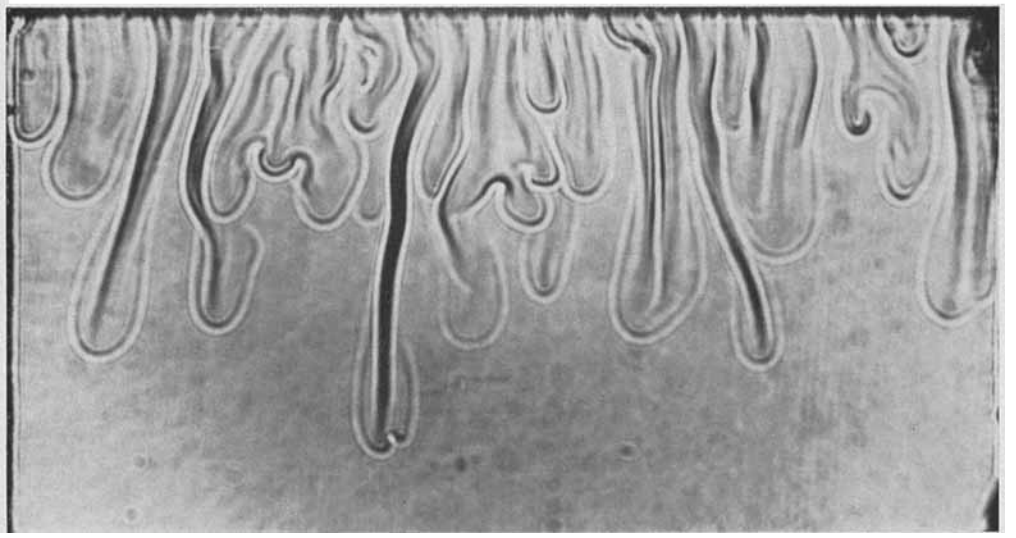

(*e*)

FIGURE 8. Convection for a cell-wall separation of 0·076 cm and salinity of 25 ‰. The horizontal field of view is 26·7 cm. Times after onset: (*a*) 45 s, (*b*) 90 s, (*c*) 135 s, (*d*) 180 s, (*e*) 225 s.